Characterization of bubble formation in microfluidic fuel cells employing hydrogen peroxide

Jin-Cherng Shyu *, Cheng-Ling Huang

Department of Mechanical Engineering, National Kaohsiung University of Applied Sciences, Kaohsiung 80778, Taiwan

A B S T R A C T

In order to examine bubble evolution and discuss the effects of bubbles effect on the performance of microfluidic fuel cells, two 1.2-mm-depth microfluidic fuel cells employing 0.1-M H_2O_2 dissolved in 0.1-M NaOH solution and 0.05-M H_2SO_4 solution as fuel and oxidant, respectively, with transparent lids having width of 1.0 mm and 0.5 mm, are fabricated in the present study for both cell performance measurement and flow visualization. The results show that the present cells operating at either a higher volumetric flow or a smaller microchannel width yield both better performance and more violent bubble growth. The bubble growth rate, Q_g, in a given microfluidic fuel cell is almost the same at different regions of that cell at a given volumetric flow rate, i.e. 10^{-5} cm^3 s^{-1} and 5×10^{-5} cm^3 s^{-1}, respectively, for cells having widths of 0.5 mm and 1.0 mm at $Q_l = 0.05$ mL min^{-1}, and slightly increases at higher volumetric flow rates. Furthermore, the present study reports approximately constant values of Q_g/C_dA at various volumetric flow rates, which are 2×10^{-2} and 5×10^{-2} cm^3 s^{-1} A^{-1}, respectively, for cells having channel widths of 0.5 mm and 1.0 mm. In addition, the 0.5-mm-wide cell has higher cell output and performs more tortuous polarization curve.

© 2010 Elsevier B.V. All rights reserved.

1. Introduction

At present, the Li-ion battery is still one of the most common power sources for portable electronic devices due to its high energy density. However, the increase in the power density of the Li-ion battery in recent years appears to be falling behind the increase in power demand of such portable electronic devices. Thus, developing reliable micro scale power sources of much higher energy density than that of Li-ion battery is of vital importance for the next generation of portable electronic devices. A micro fuel cell with aqueous fuel operated at low temperature, such as the micro direct methanol fuel cell, is considered one of the most promising substitutes for the Li-ion battery due to its higher energy density and fast fuel replenishment.

However, a common fuel cell employing a Nafion® membrane has certain intrinsic problems, such as membrane humidification, membrane degradation, and inefficient prevention of fuel crossover. Therefore, in the past few years, novel microfluidic fuel cells, also called membraneless fuel cell, which operate without a polymer electrolyte membrane by transporting liquid streams containing fuel, oxidant and/or electrolyte streams in a co-laminar configuration in a single microchannel through different inlets,

have been proposed and tested. Through the contact of the fuel and oxidant with separate catalyst-covered electrodes, both the electron-losing reaction at the anode and the electron-gaining reaction at the cathode can take place independently on the electrode surface. The half-cell reactions for both anode and cathode, incorporating the diffusive ion transportation between the electrodes assisted by the supporting electrolyte in the reactants, accomplishes the overall electrochemical reaction in such microfluidic fuel cells, thus generating electricity.

Careful examination of the literature on such microfluidic fuel cells reveals that various architectures have been presented to date, with various aqueous reactants [1,2]. However, one must observe that CO_2 gas will usually be produced at the fuel cell anode if formic acid is used as the fuel [3–6]. The anode reaction for the oxidation of formic acid is as follows:

$$HCOOH \rightarrow CO_2 + 2H^+ + 2e^- \tag{1}$$

Instead of formic acid, methanol has also been used [7,8] as fuel in similar microfluidic fuel cells in either acid or alkaline electrolyte. Under such circumstances, CO_2 gas is also produced in the anode, regardless of the electrolyte used. Among the literature, few studies [3,6] have recognized that the formation of bubbles will hinder the performance of such membraneless microfluidic fuel cells, although it has been claimed that CO_2 bubbles have not been observed in their experiments due to its high solubility in water at room temperature.

Besides CO_2, oxygen is another familiar gaseous product [9–11] of the operation of microfluidic fuel cells using hydrogen peroxide as reactant. Hasegawa et al. [9] proposed a microfluidic fuel cell having a 1000-μm-wide and 50-μm-deep microchannel employing hydrogen peroxide dissolved in both alkaline (NaOH) and acid (H_2SO_4) electrolytes as fuel and oxidant, respectively. The electron-losing reaction catalyzed by platinum at the anode of the cell is

$$H_2O_2 + OH^- \rightarrow HO_2^- + H_2O$$
$$HO_2^- + OH^- \rightarrow O_2 + H_2O + 2e^- \qquad (2)$$
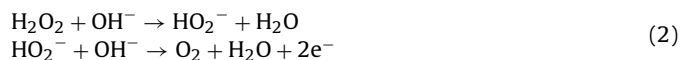
In addition, the electron-gaining reaction, also catalyzed by platinum at the cathode, is:

$$H_2O_2 + 2H^+ + 2e^- \rightarrow 2H_2O \qquad (3)$$

The H_2O_2 concentration, which is identical in both the fuel and the oxidant, was varied from 0.10 to 0.75 M. The aqueous fuel and oxidant were prepared in the molar ratio of $[NaOH]/[H_2O_2] = 1$ and $[H_2SO_4]/[H_2O_2] = 0.5$, respectively. Their measurement results showed that the cell performance increased with the increase of the reactant concentration at an extremely huge volumetric flow rate of 24 μL s^{-1}. Both maximum current density and power density of the cell at a cell voltage of 0.3 V and $[H_2O_2] = 0.75$ M were 76 mA cm^{-2} and 23 mW cm^{-2}, respectively.

Kjeang et al. [10] demonstrated a microfluidic fuel cell featuring a high-aspect-ratio T-shaped microchannel that employed hydrogen peroxide as oxidant and formic acid as fuel to experimentally study the various effects on cell performance. It was this study that recognized that the oxygen gas bubbles produced at the fuel cell cathode would be a detrimental factor in cell performance. Therefore, in order to reduce the influence of oxygen bubbles on the co-laminar flow interface for better cell performance, the authors proposed a grooved microchannel design to restrict gas bubble growth and transport the fluid to the vicinity of the cathodic active sites, and to diminish the crossover effects. The microfluidic fuel cell with a grooved microchannel produced power densities up to 30 mW cm^{-2} and a maximum current density of 150 mA cm^{-2}, operated with 2-M H_2O_2 oxidant and formic acid-based fuel at room temperature. Unfortunately, no visualization of bubble formation on the electrode surface was presented in the study to demonstrate the bubble growth process resulting from different microchannel designs.

It has been revealed [12] that bubble generation in a microchannel enhances the mixing of the parallel liquid streams in that channel. However, detailed examination of the oxygen gas bubble evolution in the anode of such a microfluidic fuel cell and its effect on the cell performance seem to be lacking. Hence, the objective of the present study is to record the oxygen bubble evolution at the anode during the electrochemical reaction and to examine the effect of bubbles on the polarization curve of microfluidic fuel cells employing H_2O_2 solution as reactant by simultaneous cell performance measurement and flow visualization. In order to achieve this goal, two microfluidic fuel cells having a 1.2-mm-deep Y-shaped microchannels with widths of 1 mm and 0.5 mm were fabricated with transparent lids for cell performance measurement and flow visualization.

2. Experimental apparatus

A schematic of the present experimental setup is shown in Fig. 1. It consists of four major components, including a microfluidic fuel cell with a Y-shaped microchannel, a fluid delivery system, and a potentiostat for cell performance measurement, as well as a high-speed video camera for image recording and acquisition.

Microfluidic fuel cells consisting of a 0.5-mm-wide or 1.0-mm-wide Y-shaped microchannel and electrode were fabricated and tested in the present study. Each sidewall of the main channel of
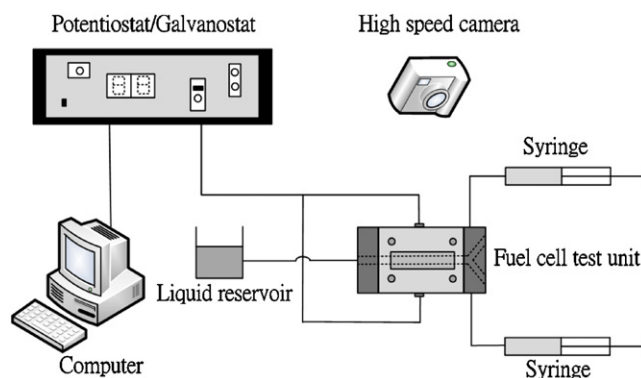

Fig. 1. Schematic diagram of the present experiment.

Table 1
Experimental conditions.

Working fluid	
Anode	Mixture of [NaOH] = 0.1 M and [H_2O_2] = 0.1 M
Cathode	Mixture of [H_2SO_4] = 0.05 M and [H_2O_2] = 0.1 M
Microchannel width (W)	0.5 mm, 1.0 mm
Microchannel length and depth	16 mm and 1.2 mm
Catalyst	Platinum
Volumetric flow rate (Q_l)	0.05, 0.1, 0.5, and 1.0 mL min^{-1}

the present microchannel was made with a platinum rod embedded in a graphite block to serve as catalyst and electrode, respectively. Both graphite blocks were separately placed on an insulated slab to form the sidewalls and the bottom wall of the microchannel. The Y-shaped microchannel was covered with a transparent polymer sheet as the top wall for flow visualization. Those parts incorporated with the microchannel inlets were clamped to form a microfluidic fuel cell capable of performing the experiment in several volumetric flow rates without liquid leakage. The microchannel depth and length of the microfluidic fuel cells were 1.2 mm and 16 mm, respectively. During the experiments, both electrodes were connected to a potentiostat/Galvanostat (Versastat II, Princeton Applied Research) to measure the voltage–current curve at room temperature and ambient pressure under stepwise potentiostatic control. The potentiostat/Galvanostat enabled a maximum voltage and current of 20 V and 2 A, respectively.

For the fluid delivery system, a syringe pump (KDS 210, KD Scientific Inc.) with two syringes was employed. Polyethylene tubing was used to deliver liquid into the microfluidic fuel cell and to guide the waste stream out of the fuel cell. Both aqueous fuel and oxidant having the same volumetric flow rate were simultaneously pumped into the microfluidic fuel cell via individual inlets. Note that the volumetric flow rate in this study represents the inlet volumetric flow of one single stream, and the total volumetric flow rate in the microchannel is twice that value.

A high-speed video camera (Fastec imaging TroubleShooter 500) was also used for flow visualization and image acquisition. The images were taken at a rate of 50 frames s^{-1} for each test of the present fuel cell.

The fuel of the present fuel cell was a mixture of NaOH and H_2O_2 solutions, while the oxidant used here was a mixture of H_2SO_4 and H_2O_2 solutions. The experimental conditions are shown in Table 1.

3. Results and discussion

The following discussions on bubble growth for all experimental conditions are based on an average current density within

Table 2
The average current density during the period of bubble volume measurement.

Microchannel width (mm)	Volumetric flow rate (mL min^{-1})	Average current density (mA cm^{-2})
0.5 mm	0.05	12.754
	0.1	25.896
	0.5	63.024
	1.0	47.7375
1.0 mm	0.05	7.788
	0.1	29.332
	0.5	4.244
	1.0	30.884

the period when the images were taken and analysed as shown in Table 2. Fig. 2 shows the process of the growth of gas bubbles on the anode surface of the microfluidic fuel cell with a microchannel width of 0.5 mm at $Q_l = 0.05$. In Fig. 2(a), it can be found that numerous tiny bubbles initially formed in the upstream region of the microchannel at a smaller average current density of 12.754 mA cm^{-2}. Subsequently, some smaller bubbles also developed in the downstream region, as shown in Fig. 2(b) and (c), and showed a fairly uniform bubble distribution over the entire electrode surface, with diverse size. Based on the visualization, it can also be observed that oxygen bubbles were likely to move due to the fluid flow and then to coalesce with other bubbles around them, forming new larger bubbles, as marked in Fig. 2(b) and (c). However, due to the occupation of the downstream electrode surface by other bubbles, the larger bubble, after coalescence, detached from the electrode surface. Once the bubbles moved downstream, new bubbles formed rapidly on the unoccupied anode surface, as shown in the front region of the marked larger bubble. Based on the present visualization, besides moving downstream, bubbles that formed on the deeper surface of the electrode would also be carried by buoyancy. The aforementioned bubble movements sometimes pushed the bubble toward the cathode surface. This is one of the reasons
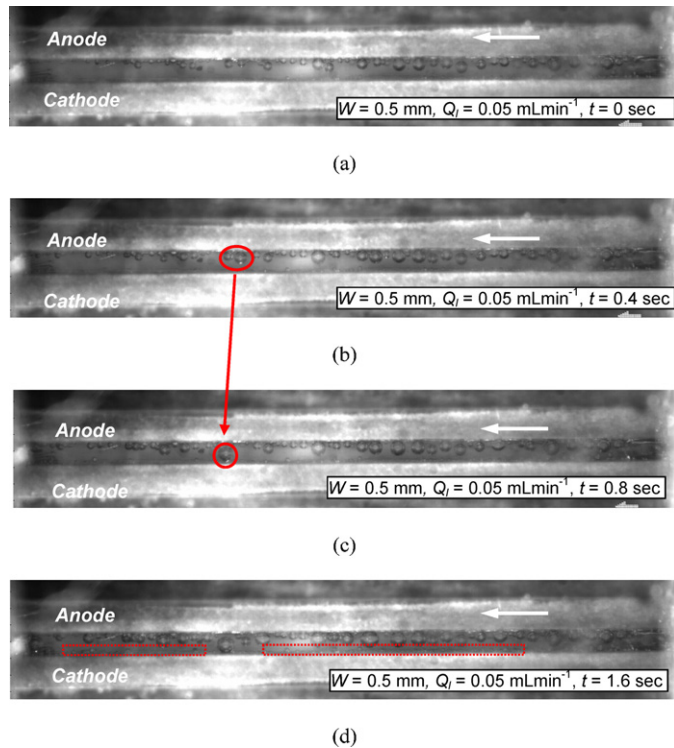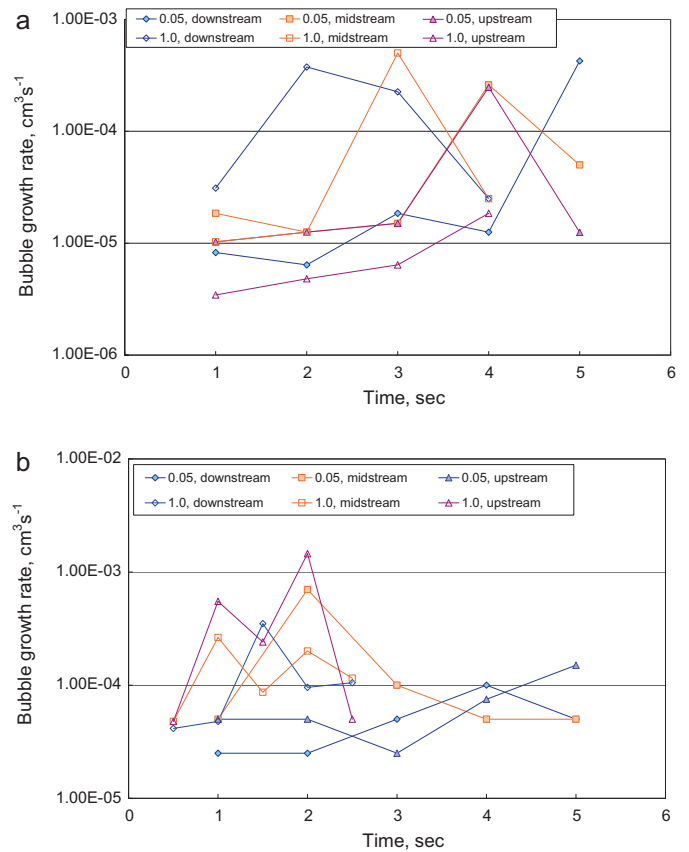

Fig. 3. Measured bubble growth rate vs. time in three distinct regions of the microchannel of the present microfluidic fuel cell at $Q_l = 0.05$ mL min^{-1} and 1.0 mL min^{-1} at (a) $W = 0.5$ mm; (b) $W = 1.0$ mm.

why bubbles can also be observed near the cathode surface in Fig. 2. In addition, some of the tiny bubbles growing on the cathode surface enclosed by the dashed line in Fig. 2(d) might be attributed to other reasons, such as the catalytic decomposition of hydrogen peroxide by platinum.

In order to analyse the bubble growth rates at different positions of the electrode, the microchannel of the microfluidic fuel cells was divided into three regions, denoted as upstream, midstream, and downstream, of equal length. One of the bubbles in each region was chosen and monitored for size variation with time. In this study, the bubble in the microchannel was in the form of a sphere if the bubble length was less than the microchannel width ($L_b \leq w$); one constrained by the sidewalls of the microchannel became a distorted sphere, being approximated as a rectangular solid with a cross-sectional area equal to that of the microchannel, if the bubble length was larger than the microchannel width ($L_b > w$), where L_b is the bubble length from the top-view image. The bubble growth rate (Q_g, cm^3 s^{-1}) is defined here as the time rate change of the bubble volume, which was calculated based on the successive images of the microchannel over several seconds during the fuel cell experiments.

The bubble growth rates at $Q_l = 0.05$ and 1.0 mL min^{-1} in three distinct regions of microchannels with widths of 0.5 mm and 1.0 mm, respectively, are shown in Fig. 3(a) and (b). Based on the observations above, it can be recognized that the rises of the curves in both figures represent the bubble coalescence, which resulted in a higher growth rate at that moment. After the coalescence, the bubble growth rate fell to a lower value. It is also shown in Fig. 3(a) and (b) that the bubbles grew in different regions of the microchannel at $Q_l = 0.05$ mL min^{-1} at an approximate rate,

Fig. 2. Successive pictures showing oxygen bubble formation at $Q_l = 0.05$ mL min^{-1} in the anode of a microfluidic fuel cell with a microchannel width of 0.5 mm: (a) 0; (b) 0.4; (c) 0.8; (d) 1.6 s.
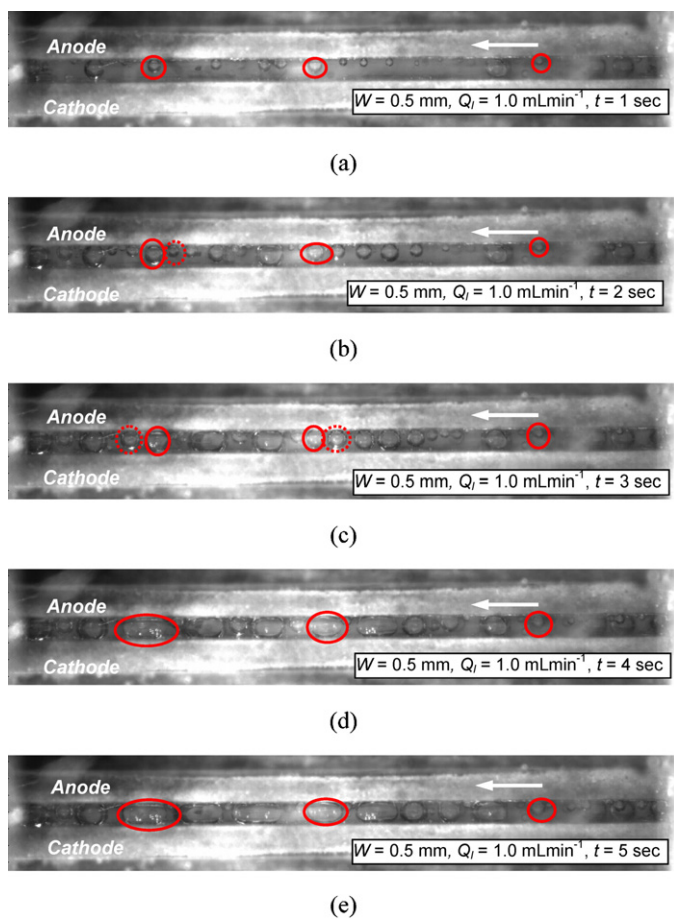
(a)

(b)

(c)

(d)

(e)

Fig. 4. Bubbles growing upstream, midstream, and downstream of the present cell having a width of 0.5 mm at $Q_l = 1.0$ mL min^{-1}, showing bubble growth and coalescence: (a) 1; (b) 2; (c) 3; (d) 4; (e) 5 s.

Fig. 5. The ratio of measured bubble growth rate to average current density at various volumetric flow rates of the microfluidic fuel cells having channel widths of 0.5 mm and 1.0 mm.

unless coalescence occurred. For example, $Q_g = 10^{-5}$ cm^3 s^{-1} and 5×10^{-5} cm^3 s^{-1} for microfluidic fuel cells with widths of 0.5 mm and 1.0 mm, respectively. In addition, comparing the bubble growth rates at $Q_l = 0.05$ mL min^{-1} and $Q_l = 1.0$ mL min^{-1}, it can be found in Fig. 3 that the bubble growth rate at $Q_l = 1.0$ mL min^{-1} was slightly higher than that at $Q_l = 0.05$ mL min^{-1}.

However, the increased rises of the curves in Fig. 3(a) and (b) at a higher volumetric flow rate of 1.0 mL min^{-1} imply that the bubble had a much greater tendency to merge with other bubbles in the vicinity at a higher volumetric flow rate. Fig. 4 shows the bubble growth process at a higher average current density, 47.74 mA cm^{-2}, and a higher volumetric flow rate, 1.0 mL min^{-1}. The coalescence of the bubble chosen for bubble volume estimation in the downstream of the microchannel, marked by a solid circle, and the bubble marked by a dashed circle in Fig. 4(b) formed a new larger bubble, indicated by a solid circle in the downstream of the microchannel in Fig. 4(c). The rise of the bubble growth rate from $t = 1$ to $t = 2$ at $Q_l = 1.0$ mL min^{-1} and microchannel width of 0.5 mm in Fig. 3 reflected the aforementioned bubble coalescence process from Fig. 4(b) and (c). Moreover, further coalescence of the bubble marked by a solid circle in Fig. 4(c) occurred with a nearby bubble, marked by a dashed circle in Fig. 4(c), thus forming a larger bubble, marked with a solid circle in Fig. 4(d). Such a process indicates another larger value at $t = 3$ of the said curve in Fig. 3(a). Similar results in different regions of the microfluidic fuel cell in Fig. 3(a) can also be observed in Fig. 4. Frequent bubble coalescence demonstrated in Fig. 4 led to several bubble slugs occupying some sections of the microchannel in Fig. 4.
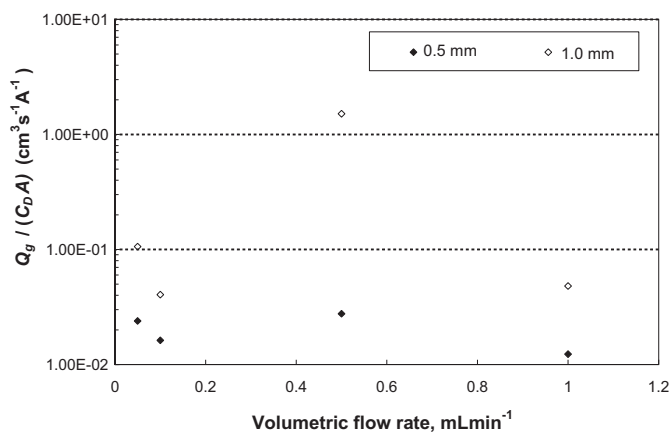
Eq. (2) expresses that a transfer of two moles of electrons accompanies the production of one mole of oxygen gas in the alkaline electrolyte in the present microfluidic fuel cell. Therefore, the oxygen generation rate (Q_g), or the oxygen bubble growth rate, can be exactly calculated at different current densities as follows,

$$Q_g = \frac{C_d A}{2F}(\text{mol/s}) = \frac{C_d A}{2F}\frac{M_g}{\rho_g}(\text{cm}^3/\text{s}) \quad (4)$$

where Q_g, C_d, A, F, M_g, and ρ_g are bubble growth rate, current density, active electrode area, Faraday constant, molecular weight of the oxygen gas, and oxygen gas density, respectively.

In addition, the molar fraction of the oxygen produced in the microfluidic fuel cell at a given current density and volumetric flow rate can be expressed as:

$$X_g = \frac{Q_g \rho_g / M_g}{(Q_l \rho_l / M_l) + (Q_g \rho_g / M_g)} \quad (5)$$

where Q_l, M_l, and ρ_l are volumetric flow rate of aqueous reactant, molecular weight of the aqueous reactant, and aqueous reactant density, respectively. The oxygen solubility in water in molar fraction is about 2.3×10^{-5} at 25 °C [13]. Oxygen gas bubbles are likely to form at a given flow rate with a current density higher than a threshold value if the molar fraction of O$_2$ estimated by Eq. (5) is higher than its solubility.

The oxygen generation rate in the present cells can be determined at the corresponding current density acquired from the measured cell current output based on Eq. (4). However, in contrast to the actual phenomenon presented in the experiment, the above calculation results indicated that no bubbles would be generated for all experimental conditions of the present cells because the oxygen gas produced would be totally dissolved in the liquid reactant. That means that the amount of oxygen gas produced in the present experiment is much more than the estimated value. This phenomenon is the same as that observed by Kjeang et al. [10].

In spite of the underestimation of the oxygen gas production, the ratio of oxygen bubble growth rate, Q_g, to the generated current, $C_d A$, should be approximately a constant expressed by Eq. (4), no matter how much current density was present during the period of bubble volume analysis. The related results are demonstrated in Fig. 5 for microfluidic fuel cells having different channel widths at various volumetric flow rates. Except for a particularly large value obtained at $Q_l = 0.5$ mL min^{-1} and a channel width of 1.0 mm, the values of average measured bubble growth rate divided by average current output were approximately constants for the present cells: 2×10^{-2} or 5×10^{-2} cm^3 s^{-1} A^{-1} for cells having channel widths of 0.5 mm and 1.0 mm, respectively. These constants reveal that the
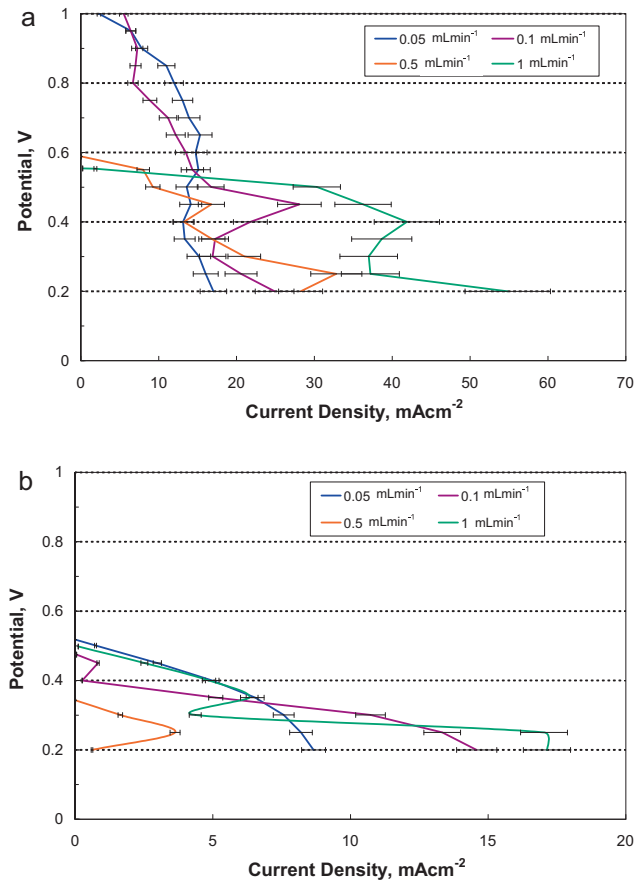
Fig. 6. The V–I curves at various Q_l of the present microfluidic fuel cells having microchannel widths of (a) 0.5 mm and (b) 1.0 mm.

oxygen bubble growth in a larger microchannel is slightly faster than that in a smaller microchannel per unit current output in the present experiment.

Fig. 6(a) and (b) shows the performance of the present fuel cell having widths of 0.5 mm and 1.0 mm, respectively, at various volumetric flow rates. Since the oxygen bubbles were observed to form on the anode surface, as shown in Fig. 2, the active sites of the electrode were partly blocked by the gas bubbles. In addition, bubbles forming in such microchannels caused an undesired mixing of the fuel and oxidant due to the growth of the bubbles. The above-mentioned effects, electrode blocking and concentration boundary layer over the electrode, would be variational due to the unsteady bubble evolution. Therefore, the unsteady oscillation of the fuel cell performance shown in Fig. 6 could likely be attributed to the formation, growth, and detachment of O_2 gas bubbles resulting from H_2O_2 oxidation on the electrodes.

Fig. 6(a) and (b) also reveals that the cell potential corresponding to zero current output might not be a fixed value at different operating conditions. The cell potential at zero current output for the present cell with a width of 1.0 mm was around 0.5 V, except in the case of the $Q_l = 0.5$ mL min^{-1}. In addition, the polarization curves in Fig. 6(b) are smoother than those in Fig. 6(a). However, for the cell having a microchannel width of 0.5 mm, the cell potential at zero current density at $Q_l = 0.05$ and 1.0 mL min^{-1}, which was larger than 1.0 V, showed a visible difference compared with that at a larger volumetric flow rate, i.e., about 0.55 V at $Q_l = 1.0$ mL min^{-1}. Consistent with the published tested results of microfluidic fuel cells that employed hydrogen peroxide as reactant [10,11], the same phenomenon was also reported in that the open circuit potential would not be a fixed value at different volumetric flow rates for

a given microchannel. In addition, the open circuit potential for the microfluidic fuel cells that would produce oxygen gas bubbles during operation tested by different research groups has a visible difference ranging from 1.1 V [10] to 0.6 V [11]. The reported range of the open circuit potential is also similar to that measured in the present study. It is possible that the oxygen gas bubbles disturb the liquid flow in the microchannel, subsequently leading to the fluctuations in the open circuit potential.

Despite the unstable cell performance and distinct cell potential at zero current output, Fig. 6(a) and (b) reveals that the increase of the volumetric flow rates of the aqueous reactant ranging from 0.05 mL min^{-1} to 1.0 mL min^{-1} usually increased the cell output. One of the major causes of the inferior performance could be the larger ohmic loss, indicated by a steeper polarization curve, at smaller volumetric flow, as shown in Fig. 6. Comparing the cell performance in Fig. 6(a) and (b) reveals that the cell with a microchannel width of 0.5 mm performed better than the cell with a width of 1.0 mm. The current densities of the 0.5-mm-width microfluidic fuel cell at 0.2 V at $Q_l = 0.05$ and 1.0 mL min^{-1} were 17.03 and 54.84 mA cm^{-2}, as shown in Fig. 6(a), while the current densities at 0.2 V of the 1.0-mm-width microfluidic fuel cell were 8.66 and 17.14 mA cm^{-2} at the same operation conditions, as shown in Fig. 6(b). In addition, the polarization curves at various flow rates of the cell having a microchannel width of 0.5 mm in Fig. 6(a) are usually more tortuous than those of the cell having a microchannel width of 1.0 mm in Fig. 6(b). It has been reported [10,11] that the current density of similar microfluidic fuel cells can be enhanced by increasing the volumetric flow rate or Reynolds number. Also, higher current output yielded a greater amount of oxygen gas in the present study, as shown in Fig. 5. Therefore, more tortuous polarization curves for the present cells with either the smaller channel width in Fig. 6(a) or the higher volumetric flow rates in Fig. 6(a) and (b) might be attributed to oxygen bubble formation during the electric generation process, which disturbs the co-laminar stream in the microchannel [10].

4. Conclusions

In order to examine the bubble evolution on a single electrode in microfluidic fuel cells and discuss its effect on cell performance, an experiment was conducted to simultaneously measure the cell performance and perform flow visualization. Two microfluidic fuel cells, whose microchannel widths were 0.5 mm and 1.0 mm, respectively, and microchannel depths were 1.2 mm, using 0.1-M H_2O_2 solution mixed with 0.1-M NaOH and 0.05-M H_2SO_4 as fuel and oxidant, respectively, were tested in the present study. The experiment was carried out at various volumetric flow rates, from 0.05 mL min^{-1} to 1.0 mL min^{-1}.

The results showed that both unstable electrical output and O_2 gas bubbles on the anode surface were indeed generated during the operation of the cells. Compared with the bubble growth at smaller volumetric flow rates, cells operating at higher volumetric flow rates showed both more frequent coalescence of the O_2 gas bubbles with other bubbles in the vicinity, and slightly higher bubble growth rates. In addition, it was found that the ratio of average measured bubble growth rate to average current output, $Q_g/C_d A$, was approximately a constant for the present microfluidic fuel cells tested at various volumetric flow rates, which were 2×10^{-2} and 5×10^{-2} cm^3 s^{-1} A^{-1} for microfluidic fuel cells having channel widths of 0.5 mm and 1.0 mm, respectively.

In addition, cells operating at either a higher flow rate or with a smaller microchannel width resulted in both higher current output and more unstable polarization curve in the present tests. The current densities of the 0.5-mm-wide microfluidic fuel cell at 0.2 V at $Q_l = 0.05$ and 1.0 mL min^{-1} were 17.03 and 54.84 mA cm^{-2}, as

shown in Fig. 6(a), while the current densities at 0.2 V of the 1.0-mm-width microfluidic fuel cell were 8.66 and 17.14 mA cm^{-2} at the same operation conditions, as shown in Fig. 6(b).

Acknowledgement

References

[1] E. Kjeang, N. Djilali, D. Sinton, J. Power Sources 186 (2009) 353–369.
[2] J.C. Shyu, C.S. Wei, C.J. Lee, C.C. Wang, Appl. Therm. Eng. 30 (2010) 1863–1871.
[3] E.R. Choban, L.J. Markoski, A. Wieckowski, P.J.A. Kenis, J. Power Sources 128 (2004) 54–60.
[4] J.L. Cohen, D.A. Westly, A. Pechenikc, H.D. Abruňa, J. Power Sources 139 (2005) 96–105.
[5] R.S. Jayashree, L. Gancs, E.R. Choban, A. Primak, D. Natarajan, L.J. Markoski, P.J.A. Kenis, J. Am. Chem. Soc. 127 (2005) 16758–16759.
[6] M.H. Sun, G.V. Casquillas, S.S. Guo, J. Shin, H. Ji, O. Ouyang, Y. Chen, Microelectron. Eng. 84 (2007) 1182–1185.
[7] E.R. Choban, J.S. Spendelow, L. Gancs, A. Wieckowski, P.J.A. Kenis, Electrochim. Acta 50 (2005) 5390–5398.
[8] E.R. Choban, P. Waszczuk, P.J.A. Kenis, Electrochem. Solid State 8 (2005) A348–A352.
[9] S. Hasegawa, K. Shimotani, K. Kishi, H. Watanabe, Electrochem. Solid State 8 (2005) A119–A121.
[10] E. Kjeang, A.G. Brolo, D.A. Harrington, N. Djilali, D. Sinton, J. Electrochem. Soc. 154 (2007) B1220–B1226.
[11] A. Li, S.H. Chan, N.T. Nguyen, J. Micromech. Microeng. 17 (2007) 1107–1113.
[12] J.C. Shyu, C.J. Lee, C.S. Wei, J. Micro-Nanolithogr. MEMS MOEMS 8 (2009) 021105.
[13] D.R. Lide, CRC Handbook of Chemistry and Physics, CRC Press, Boca Raton, 1992.